

Optical rogue waves and W-shaped solitons in the multiple self-induced transparency system

Xin Wang^{a*}, Chong Liu^b

^a*Department of Mathematics, Zhongyuan University of Technology, Zhengzhou, 450007, China*

^b*School of Physics, Northwest University, Xi'an, 710069, China*

Abstract

We study localized nonlinear waves on a plane wave background in the multiple self-induced transparency (SIT) system, which describes an important enhancement of the amplification and control of optical waves compared to the single SIT system. A hierarchy of exact multiparametric rational solutions in a compact determinant representation are presented. We demonstrate that, this family of solutions contains known rogue wave solution and unusual W-shaped soliton solution, which strictly corresponds to the linear stability analysis that involves modulation instability and stability regimes in the low perturbation frequency region. State transitions between rogue waves and W-shaped solitons as well as the higher-order nonlinear superposition modes are revealed by the suitable choice for the background wavenumber of electric field component. In particular, our results show that, the multiple SIT system admits stationary and nonstationary nonlinear modes in contrast to the results in the single SIT system. Correspondingly, the important characteristics of the nonlinear waves including trajectories and spectrum are revealed in detail.

Keywords: Multiple self-induced transparency system; rogue wave; soliton; state transition; dynamics property.

1. Introduction

Fiber optic communication has been a topic of considerable interest with important applications in theoretical and experimental physics [1]. Dissipation and dispersion effects are the main hindrance for the signal propagation through optical fibers [2]. To deal with this, one type of optical soliton that is described by the nonlinear Schrödinger (NLS) equation, where the group velocity dispersion in the light pulse wave guide can be balanced by the self-phase modulation, has been extensively investigated [3]. The other type of coherent optical soliton that is based on self-induced transparency (SIT) firstly discovered by McCall and Hahn in a pure two-level atomic transition system, has also received long-running attention [4].

It is discovered by Lamb that the SIT system (or Maxwell-Bloch equations) [5]

$$E_z = \langle p \rangle, \quad (1a)$$

$$p_t = EN + 2i\omega p, \quad (1b)$$

$$N_t = -2(Ep^* + E^*p). \quad (1c)$$

serves as a basic model to govern the SIT phenomenon in a two-level medium. Here, E is the slowly

*Corresponding author.

Email address: wangxinlinzhou@163.com (Xin Wang^{a*})

varying complex envelope of electric field, $\langle p \rangle$ denotes the average polarization

$$\langle p \rangle = \int_{-\infty}^{\infty} p(t, z; \omega) g(\omega) d\omega, \quad \int_{-\infty}^{\infty} g(\omega) d\omega = 1,$$

where $g(\omega)$ is the normalized probability density, N stands for the population inversion between two level, and the index $*$ represents complex conjugation. The above system can be immediately converted to the AB system in geophysical fluid dynamics [6] and sine-Gordon equation in differential geometry [7]. Thus far, there has been a surge of great many reports on the integrability and analytic solution of system (1). For example, the inverse scattering theory for solving the the general initial value problem was established by Ablowitz and Gabitov et al. [8, 9], and the Darboux transformation (DT) for finding the soliton solution, exulton-like solution and rational solution was constructed by Matveev and Salle [10]. In particular, more recently, rogue wave solution of system (1) or AB system has been widely researched [11–14].

Remarkably, a significant enhancement of the amplification and control of the optical soliton in system (1) can be achieved if the single SIT system is generalized to the multiple case. In this connection, Kundu considered a multiple SIT system [15]:

$$E_z = \langle p \rangle, \tag{2a}$$

$$p_t = -e + EN + 2i\omega p, \tag{2b}$$

$$N_t = -2(Ep^* + E^*p), \tag{2c}$$

$$e_t = -2EM + 2i\omega e, \tag{2d}$$

$$M_t = -Ee^* + E^*e. \tag{2e}$$

Here, e and M are the new introduced induced polarization and population inversion, respectively. When taking $e \rightarrow 0$ and $M \rightarrow 0$, system (2) is reduced to the single SIT system (1). The complete integrability and soliton solution of system (2) have been discussed in Kundu' work.

Nevertheless, to our knowledge, optical rogue waves and W-shaped solitons in system (2) have not been reported anywhere. As is known to all, rogue waves are defined as waves having large amplitudes and emerging randomly in the particular dynamic system with low probability [16]. The rogue wave phenomena were originally applied to describe the unexpected appearance of huge and short-lived catastrophic waves on the ocean, but now have rapidly spread to a wide range of physical systems including optical fibres [17], Bose-Einstein condensates [18], plasmas [19], cold atoms [20] and so on.

The simplest simulation of a single rogue wave in mathematics is the Peregrine soliton, which is a rational solution describing an ‘‘amplitude peak’’ isolated in both space and time of the NLS equation [21]. Subsequently, it is demonstrated that the intricate and diverse types of higher-order rogue waves which are constructed as the nonlinear superposition or combination of the first-order Peregrine rogue waves can exist in the NLS equation [22, 23]. However, it is necessary to say that, in order to model the complicated rogue wave phenomena in various physical systems in a relevant way, one should transcend the standard NLS description. Consequently, some important NLS-type equations (e.g. Hirota equation and Sasa-Satsuma equation) with higher-order and/or dissipative effects [24, 25], and the coupled-wave systems (e.g. Manakov system and coupled Hirota equations) with interacting wave components of different amplitudes and frequencies [26–28] have been of continued interest. Most recently, Akhmediev and one of the authors Liu show that the higher-order integrable perturbations and coupled-wave interaction can indeed generate state transition effects from breather/rogue wave to W-shaped soliton [29–32].

The purpose of this paper is mainly concentrated on two aspects: (1) we construct an N th-order rational solution in a compact determinant representation by taking advantage of the generalized DT approach [33–36]; (2) With the aid of the analytical rational solution and modulation instability (MI), dynamics of the optical rogue waves, as well as the stationary and nonstationary W-shaped solitons from first to third order are presented. In particular, it is importantly found that, the nonstationary W-shaped solitons can only exist in the multiple SIT system, while for the single system they are impossible to appear.

Our paper is organized as follows: section 2 derives a compact determinant form for an N th-order rational solution by using the generalized DT [33–36]. In section 3, dynamics of different kinds of rogue waves and W-shaped solitons, and the important state transition is revealed. Moreover, the trajectories of the rogue waves are shown. In section 4, spectrum and energy of the rogue wave solution are given. At last, the conclusion and some discussion are given.

2. N th-order rational solution

Our starting point is the Lax pair of system (2), which can be constructed in the form

$$\Psi_t = U\Psi, \quad (3)$$

$$\Psi_z = V\Psi, \quad (4)$$

where

$$U = i \begin{pmatrix} \zeta & 0 \\ 0 & -\zeta \end{pmatrix} + \begin{pmatrix} 0 & E \\ -E^* & 0 \end{pmatrix},$$

$$V = -\frac{1}{4(\zeta - \omega)^2} \begin{pmatrix} M & e \\ -e^* & -M \end{pmatrix} + \frac{1}{4i(\zeta - \omega)} \begin{pmatrix} N & -2p \\ -2p^* & -N \end{pmatrix}.$$

Here, ζ is the complex eigenvalue parameter. It is readily to prove that system (2) can be exactly reproduced from the compatibility condition $U_z - V_t + UV - VU = 0$.

To proceed, let $\Psi_1 = (\psi_1, \phi_1)^T$ be a basic solution of Eqs. (3) and (4) with $E = E[0]$, $p = p[0]$, $N = N[0]$, $e = e[0]$, $M = M[0]$ and $\zeta = \zeta_1$, then one can verify that the following gauge transformation

$$\Psi[1] = T\Psi, \quad T = I + \frac{\zeta_1^* - \zeta_1}{\zeta - \zeta_1^*} \frac{\Psi_1 \Psi_1^\dagger}{\Psi_1^\dagger \Psi_1}, \quad (5)$$

$$E[1] = E - 2i(\zeta_1^* - \zeta_1) \frac{\psi_1 \phi_1^*}{|\psi_1|^2 + |\phi_1|^2}, \quad (6)$$

is just the classical DT of the Lax pair system. Here, \dagger denotes Hermite conjugation. We point out that, in this paper, we only pay our attention to the rational solutions including rogue wave solution and W-shaped soliton solution of the electric field, i.e. the E component. For the p , N , e and M components, we omit the results, since their new potentials can be directly derived from the differential and/or integral calculations of $E[1]$ by virtue of the original system, and the corresponding rogue waves and W-shaped solitons in these components are similar to the ones in E component with the same initial excitations.

After that, we introduce a general plane-wave solution of system (2), that is

$$E[0] = ce^{i\theta}, \quad p[0] = icbe^{i\theta}, \quad \theta = at + bz, \quad N = d_0,$$

$$e[0] = c(ab - 2b\omega + d_0)e^{i\theta}, \quad M[0] = -1/2i(ab - 2b\omega + d_0)(a - 2\omega). \quad (7)$$

Here, c , a and b represent the background amplitude, frequency and wave number of the electric field, respectively, and d_0 is a real constant.

Next, in view of the classical DT (5), (6) and its higher-degree generalized form by taking the limit technique, we can directly work out a unified N th-order rational solution of the following compact form as

$$E[N] = \left(1 - 2i \frac{\det(H_1)}{\det(H)} \right) ce^{i\theta}, \quad (8)$$

where

$$H = \begin{pmatrix} H[1, 1] & H[1, 2] & \cdots & H[1, N] \\ H[2, 1] & H[2, 2] & \cdots & H[2, N] \\ \vdots & \vdots & \ddots & \vdots \\ H[N, 1] & H[N, 2] & \cdots & H[N, N] \end{pmatrix},$$

$$H_1 = \begin{pmatrix} H[1, 1] & H[1, 2] & \cdots & H[1, N] & \phi_1^{[0]*} \\ H[2, 1] & H[2, 2] & \cdots & H[2, N] & \phi_1^{[1]*} \\ \vdots & \vdots & \ddots & \vdots & \vdots \\ H[N, 1] & H[N, 2] & \cdots & H[N, N] & \phi_1^{[N-1]*} \\ \psi_1^{[0]}/c & \psi_1^{[1]}/c & \cdots & \psi_1^{[N-1]}/c & 0 \end{pmatrix},$$

with

$$H[i, j] = \frac{1}{2(i-1)!2(j-1)!} \frac{\partial^{2(i+j-2)}}{\partial f^{2(j-1)} \partial f^{*2(i-1)}} \frac{\psi_1 \psi_1^* + \phi_1 \phi_1^*}{2ic(1+f^2+f^{*2})} \Big|_{f, f^* \rightarrow 0},$$

$$\psi_1^{[l]} = \frac{1}{2l!} \frac{\partial^{2l} \psi_1}{\partial f^{2l}} \Big|_{f \rightarrow 0}, \quad \phi_1^{[l]} = \frac{1}{2l!} \frac{\partial^{2l} \phi_1}{\partial f^{2l}} \Big|_{f \rightarrow 0}, \quad l = 0, 1, \dots, N-1,$$

being denoted by

$$\psi_1 = (C_2 e^A - C_1 e^{-A}) e^{\frac{i}{2}\theta},$$

$$\phi_1 = (C_1 e^A - C_2 e^{-A}) e^{-\frac{i}{2}\theta},$$

such that the coefficients satisfy

$$C_1 = \frac{(1 + 2f^2 + 2f\sqrt{1+f^2})^{\frac{1}{2}}}{2f\sqrt{1+f^2}}, \quad C_2 = \frac{(1 + 2f^2 - 2f\sqrt{1+f^2})^{\frac{1}{2}}}{2f\sqrt{1+f^2}},$$

and

$$A = 2cf\sqrt{1+f^2} \left[t - \frac{\left(ab - 4b\omega + d_0 + 2b\left(\frac{a}{2} + ic + 2icf^2\right) \right)}{4\left(\frac{a}{2} + ic + 2icf^2 - \omega\right)^2} z + \sum_{i=1}^{N-1} s_i f^{2i} \right].$$

Here, f is a complex small parameter, and s_i are the complex constants.

3. MI, rogue wave and W-shaped soliton

3.1. Modulation instability

It has been recently realized that rogue wave exists only in the MI subregion with zero-frequency [37], and the state transition between rogue wave and W-shaped soliton arises from the attenuation

of MI growth rate [30, 38]. Hence for the sake of using Eq. (8) to describe the dynamics of rogue wave and W-shaped soliton, we first perform the standard MI analysis to reveal the MI characteristic arising from the coupling effects.

To this end, we consider the following equivalent form of system (2)

$$E_{ttz} = 4i\omega E_{tz} + (EN)_t + 4\omega^2 E_z + 2EM - 2i\omega EN, \quad (9a)$$

$$N_t = -2(|E|^2)_z, \quad (9b)$$

$$M_t = EE_{tz}^* - E^* E_{tz} + 2i\omega(|E|^2)_z, \quad (9c)$$

where the p and e components are eliminated by substituting Eqs. (2a) and (2b) into Eq. (2d).

At this point, a perturbed nonlinear background may be given by

$$E = ce^{i\theta}(1 + u), \quad N = d_0 + v, \quad M = -1/2i(ab - 2b\omega + d_0)(a - 2\omega) + iw,$$

where $u(t, z)$, $v(t, z)$ and $w(t, z)$ are the small perturbed functions and fulfil a linear equation group. Let

$$u = f_+ e^{i\kappa(t-\Omega z)} + f_- e^{-i\kappa(t-\Omega^* z)}, \quad v = g e^{i\kappa(t-\Omega z)} + g^* e^{-i\kappa(t-\Omega^* z)}, \quad w = h e^{i\kappa(t-\Omega z)} + h^* e^{-i\kappa(t-\Omega^* z)},$$

where κ and Ω are assumed to be real and complex. Embedding them into system (9) and taking the linear part for $\alpha = (f_+, f_-, g, h)^T$, we have the algebraic equation $B\alpha = 0$, where

$$\begin{aligned} B_{11} &= -\Omega\kappa^3 + (-2a\Omega + 4\Omega\omega + b)\kappa^2 + (-a^2\Omega + 4a\Omega\omega - 4\Omega\omega^2 + 2ab - 4b\omega + d_0)\kappa, \\ B_{22} &= \Omega\kappa^3 + (-2a\Omega + 4\Omega\omega + b)\kappa^2 + (a^2\Omega - 4a\Omega\omega + 4\Omega\omega^2 - 2ab + 4b\omega - d_0)\kappa, \\ B_{31} &= c^2\Omega\kappa^2 + (ac^2\Omega - 2c^2\Omega\omega - bc^2)\kappa, \quad B_{32} = -c^2\Omega\kappa^2 + (ac^2\Omega - 2c^2\Omega\omega - bc^2)\kappa, \\ B_{12} &= B_{21} = B_{33} = B_{44} = 0, \quad B_{14} = B_{24} = 2, \quad B_{41} = B_{42} = -2ic^2\Omega\kappa, \\ B_{34} &= -\kappa, \quad B_{43} = i\kappa, \quad B_{13} = \kappa + a - 2\omega, \quad B_{23} = -\kappa + a - 2\omega. \end{aligned}$$

Solving $\det(B) = 0$ we get the MI growth rate

$$G = |\text{Im}\{\Omega\}| = \frac{\sqrt{4c^2 - \kappa^2}}{(\kappa^2 - a^2 + 4a\omega - 4c^2 - 4\omega^2)^2} |(\kappa^2 - 3a^2 + 12a\omega - 4c^2 - 12\omega^2)b - 2(a - 2\omega)d_0|. \quad (10)$$

Thus, it is easy to find that the MI exists in the region $-2c < \kappa < 2c$. Particularly, the modulation stability (MS) regions can be acquired analytically

$$b_s = \frac{2(a - 2\omega)d_0}{\kappa^2 - 3a^2 + 12a\omega - 4c^2 - 12\omega^2}. \quad (11)$$

The above MS representation depends on the background amplitude c , the frequency a , the constants d_0 and ω , and the perturbation frequency κ . In the following, we will show that once the MI growth rate attenuates to zero in the zero-frequency MS region, i.e. $b = b_s|_{\kappa=0}$, a transition between the rogue wave and W-shaped soliton occur.

3.2. Rogue wave

By utilizing Eq. (8) with $N = 1$, we obtain the first-order rational solution which has the form

$$E[1] = ce^{i\theta} \frac{F_1 + iG_1}{D_1}, \quad (12)$$

where

$$\begin{aligned}
F_1 &= -4(a^2 - 4a\omega + 4c^2 + 4\omega^2)^2 c^2 t^2 + 8(2a^3 b - 12a^2 b\omega + 24ab\omega^2 - 16b\omega^3 + a^2 d_0 - 4ad_0\omega \\
&\quad - 4c^2 d_0 + 4d_0\omega^2) c^2 z t - 4(4a^2 b^2 - 16ab^2\omega + 4b^2 c^2 + 16b^2\omega^2 + 4abd_0 - 8bd_0\omega + d_0^2) c^2 z^2 \\
&\quad + 3(a^2 - 4a\omega + 4c^2 + 4\omega^2)^2, \\
G_1 &= -16(3a^2 b - 12ab\omega + 4bc^2 + 12b\omega^2 + 2ad_0 - 4d_0\omega) c^2 z, \\
D_1 &= 4(a^2 - 4a\omega + 4c^2 + 4\omega^2)^2 c^2 t^2 - 8(2a^3 b - 12a^2 b\omega + 24ab\omega^2 - 16b\omega^3 + a^2 d_0 - 4ad_0\omega \\
&\quad - 4c^2 d_0 + 4d_0\omega^2) c^2 z t + 4(4a^2 b^2 - 16ab^2\omega + 4b^2 c^2 + 16b^2\omega^2 + 4abd_0 - 8bd_0\omega + d_0^2) c^2 z^2 \\
&\quad + (a^2 - 4a\omega + 4c^2 + 4\omega^2)^2.
\end{aligned}$$

Here we remark that the above rational solution contains two types of localized waves, i.e., (i) rogue wave with $b \neq b_s|_{\kappa=0}$ and (ii) W-shaped soliton with $b = b_s|_{\kappa=0}$. Remarkably, this family of solutions contains known rogue wave solution and unusual W-shaped soliton solution, which strictly corresponds to the above linear stability analysis that involves modulation instability and stability regimes in the low perturbation frequency region.

We first show the dynamics of the rogue wave. In the case of $b \neq b_s|_{\kappa=0}$, Eq. (12) corresponds to the celebrated “eye”-shaped (one hump and two valleys near $z = 0$) rogue wave. By using the trace analysis method, we can define the motion of the rogue wave’ hump precisely

$$T_h = Kz, \quad (13)$$

where

$$K = \frac{2(a - 2\omega)^3 b + (a - 2c - 2\omega)(a + 2c - 2\omega)d_0}{(a^2 - 4a\omega + 4c^2 + 4\omega^2)^2},$$

and the motions of its two valleys

$$T_v = \frac{K_1 \pm 2\sqrt{K_2}}{4c(a^2 - 4a\omega + 4c^2 + 4\omega^2)^2}, \quad (14)$$

where

$$\begin{aligned}
K_1 &= 4(2a^3 b - 12a^2 b\omega + 24ab\omega^2 - 16b\omega^3 + a^2 d_0 - 4ad_0\omega - 4c^2 d_0 + 4d_0\omega^2) cz, \\
K_2 &= 48(3a^2 b - 12ab\omega + 4bc^2 + 12b\omega^2 + 2ad_0 - 4d_0\omega)^2 c^4 z^2 + 3(a^2 - 4a\omega + 4c^2 + 4\omega^2)^4.
\end{aligned}$$

Solving $K = 0$ leads to

$$b = -\frac{(a - 2c - 2\omega)(a + 2c - 2\omega)d_0}{2(a - 2\omega)^3}.$$

In this situation, we exhibit that in Fig. 1(a), there are one hump and two valleys in the temporal-spatial plane. The maximum amplitude of the rogue wave is 3 and is localized at $(0, 0)$, and the minimum amplitude of it is 0 and arrives at $(\pm\sqrt{3}/2, 0)$. Moreover, it is obvious to see that in Fig. 1(b), the “ridge” of the rogue wave is vertical to the t axis, and the trajectories of the two valleys look like an “X” shape. The rogue wave at this point is nothing but the standard Peregrine rogue wave in the NLS equation [35].

When setting

$$b \neq -\frac{(a - 2c - 2\omega)(a + 2c - 2\omega)d_0}{2(a - 2\omega)^3}$$

such that K is not equal to 0. It is displayed that in Fig. 2(a), the basic shape of the rogue wave is

unchanged, however, we show that the “ridge” of the rogue wave at this time is distinctly tilted to the t axis, and its skew angle is $\arctan K^{-1}$, see Fig. 2(b). The analogous phenomena produced by the higher-order effects have been comprehensively studied for rogue waves in the Hirota equation [24], Sasa-Satsuma equation [25] and Kundu-Eckhaus equation [36, 39], while for the coupled system without any higher-order terms they have been rarely reported.

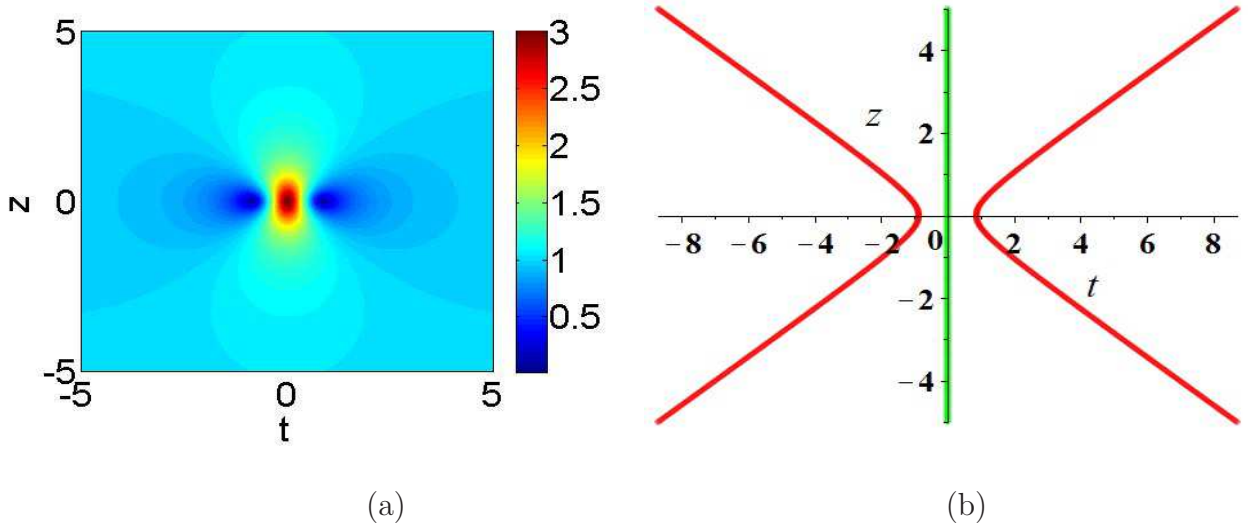


Fig. 1: (a) Density plot and (b) trace of the first-order rogue wave given by Eq. (12) with $a = 1, b = 3/2, c = 1, d_0 = 1, \omega = 0$. The green and red line correspond to the trajectories of the rogue wave’ hump and valleys, respectively. This holds for the other pictures in this paper.

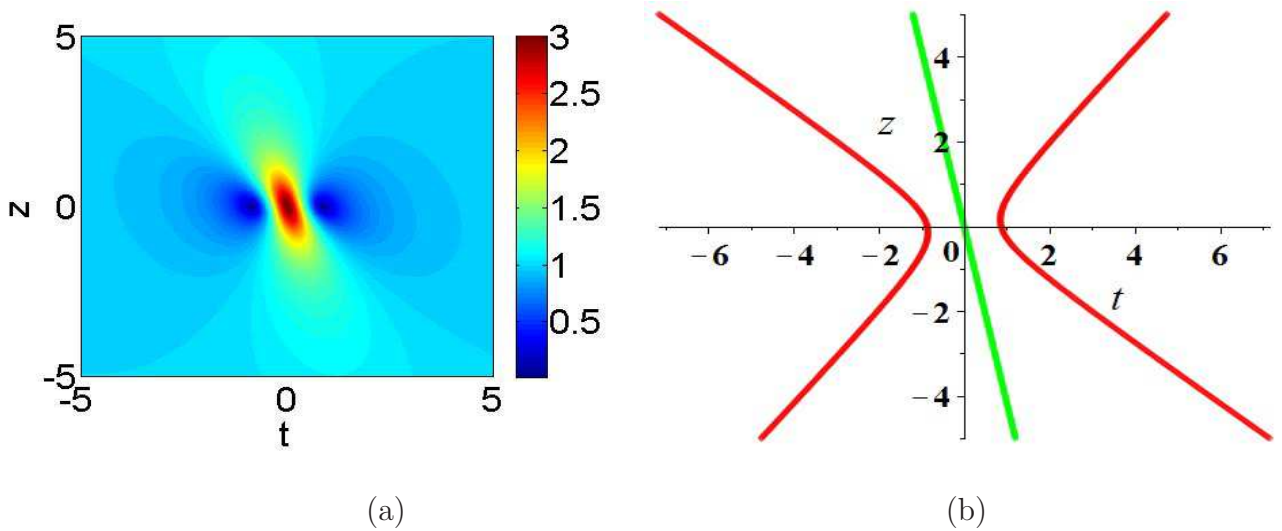


Fig. 2: (a) Density plot and (b) trace of the first-order rogue wave given by Eq. (12) with $a = 1, b = -3/2, c = 1, d_0 = 1, \omega = 0$.

Next, following the general rational solution (8) with $N = 2$, one can end up with the second-order rogue wave solution. Since the expression of the higher-order rogue wave solution involving several free parameters is very cumbersome, here we only write down a special representation of it that features fundamental pattern under the choice of $a = 1, c = 1, d_0 = 1, \omega = 0$ and $s_1 = 0$, namely,

$$E[2] = e^{i\theta} \frac{F_2 + iG_2}{D_2}, \quad (15)$$

where F_2 , D_2 and G_2 are the rational polynomials, see appendix A.

At this stage, it is apparent that there remains only one free parameter b in the above solution. The dynamics and trace characteristics of the rogue waves described by Eq. (15) with different choices of b are presented in Figs. 3 and 4. The maximum amplitude of the second-order rogue wave is 5 and occurs at $(0, 0)$. We observe that like the first-order rogue wave in Fig. 2(a), when choosing $b = -3/2$ as an example to ensure that $K \neq 0$, the “ridge” of the second-order rogue wave in Fig. 4(a) is also significantly tilted to the t axis.

As a matter of fact, we notice that, when taking $t \rightarrow \infty$ and $z \rightarrow \infty$, the trace of the higher-order rogue wave is asymptotic to that of the first-order rogue wave under the same initial excitations. For instance, in Figs. 3(b) and 4(b), when we choose the temporal and spacial intervals large enough, the traces shown in these two figures would just be contracted into the “X” shape given in Figs. 1(b) and 2(b). Thus, the skew angle of the “ridge” of the higher-order rogue wave is actually determined by that of the first-order rogue wave under the same initial excitations, i.e. the value of $\arctan K^{-1}$.

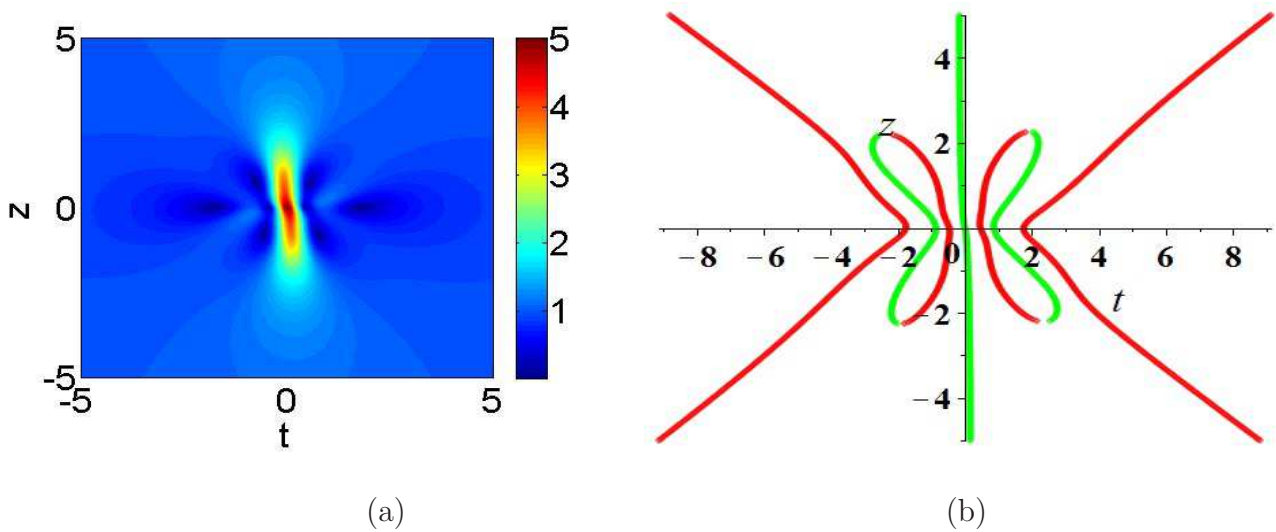


Fig. 3: (a) Density plot and (b) trace of the second-order rogue wave of fundamental pattern given by Eq. (15) with $b = 3/2$.

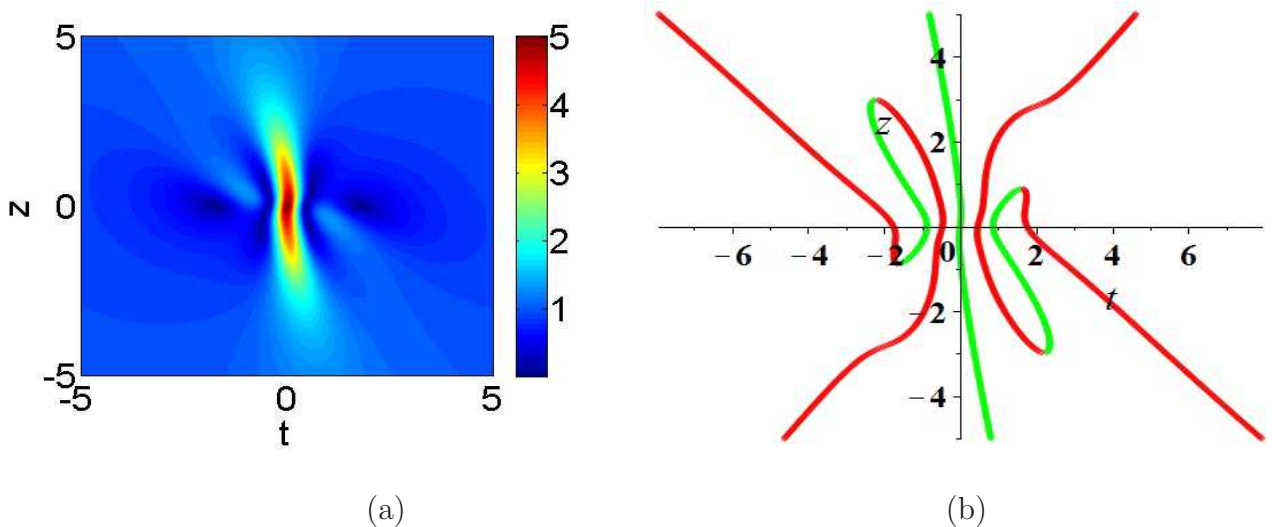


Fig. 4: (a) Density plot and (b) trace of the second-order rogue wave of fundamental pattern given by Eq. (15) with $b = -3/2$.

Hereby, we need to point out that, unlike the trace of the first-order rogue wave, the expressions of the trajectories of the humps and valleys of the second- or higher-order rogue wave can not be explicitly calculated, since the complicated high-order algebraic equation emerges in these extreme points. Consequently, in our paper, we employ the numerical method to describe the traces of the higher-order rogue waves, namely, the trajectories of the extreme points in the expressions of the higher-order rogue wave solutions.

On the other hand, when letting $s_1 \neq 0$, the fundamental second-order rogue wave can be separated into three first-order rogue waves distributing with a triangle, see Fig. 5. As is confirmed in Fig. 5(b), when choosing the value of b satisfying $K \neq 0$, the “ridge” of each of the rogue waves is tilted to the t axis. Additionally, one can also find that rogue waves in Fig. 5(b) are expanded in the z dimension, the humps in Fig. 5(a) are localized at $(-2.0173, 3.6432)$, $(4.2172, 0)$ and $(-1.9832, -3.5864)$, while in Fig. 5(b), the corresponding coordinates become $(-3.2514, 5.1937)$, $(4.2172, 0)$ and $(-0.7858, -5.3658)$.

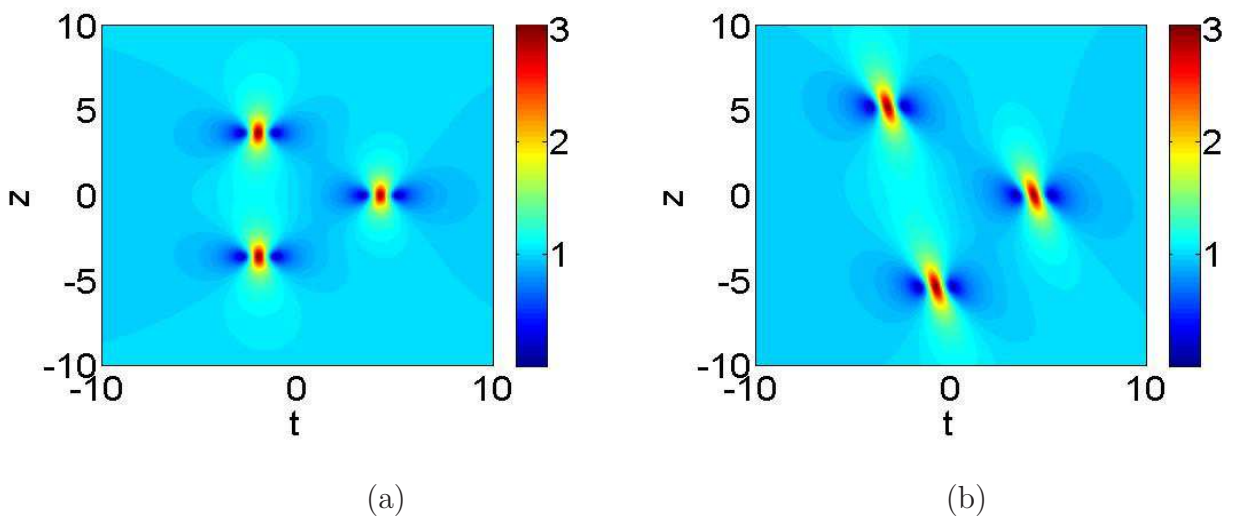


Fig. 5: (a), (b) Density plots of the second-order rogue waves of triangular pattern by choosing $b = 3/2$ and $b = -3/2$ with $a = 1, c = 1, d_0 = 1, \omega = 0, s_1 = 100$.

Afterwards, by choosing the adequate free parameters s_1 and s_2 , we can show the evolution plots of the third-order rogue waves of fundamental, triangular and circular patterns, respectively. Here, we completely refrain from giving the concrete expressions of the burdensome rational polynomials, which can be directly constructed by means of Eq. (8) with $N = 3$.

As are depicted in Figs. 6 and 7, by taking $s_1 = 0$ and $s_2 = 0$, the third-order rogue waves of fundamental pattern are shown. The maximum amplitude of the third-order rogue wave is 7 and appears at $(0, 0)$. Meanwhile, when selecting $s_1 \neq 0, s_2 = 0$ or $s_1 = 0, s_2 \neq 0$, the fundamental third-order rogue wave can split into six first-order rogue waves arraying with a triangle or a ring, respectively, see Figs. 8 and 9. Likewise, it is clearly observed that the “ridge” of each of the rogue waves in Figs. 7(a), 8(b) and 9(b) with $b = -3/2$ is tilted to the t axis in contrast with the same initial excitations except $b = 3/2$, and the range of the appearance for these rogue waves in the z dimension is notably expanded. For example, the maximum amplitudes of the six first-order rogue waves in Fig. 8(a) are localized at $(-3.5291, 6.6662)$, $(2.0912, 3.3385)$, $(-3.9545, 0)$, $(7.6248, 0)$, $(2.0701, -3.2792)$ and $(-3.4100, -6.4934)$, while in Fig. 8(b), the rogue waves are distinctly expanded in the z dimension, the corresponding coordinates turn into $(-5.7003, 9.2761)$, $(0.8638, 4.8039)$, $(-3.9545, 0)$, $(7.6248, 0)$, $(3.2612, -4.9716)$ and $(-1.3502, -9.8189)$.

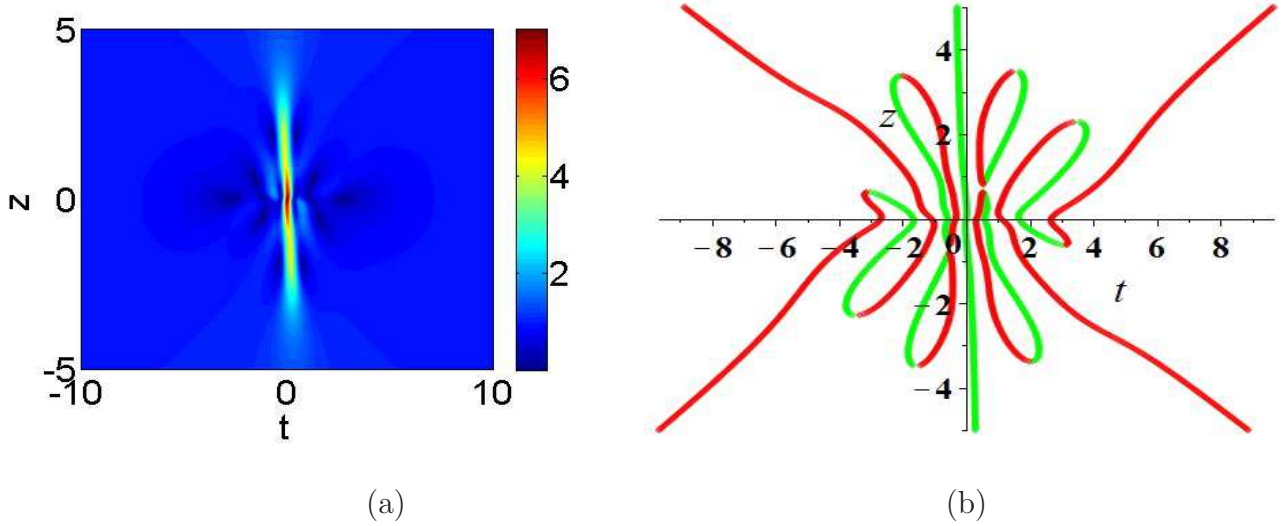


Fig. 6: (a) Density plot and (b) trace of the third-order rogue wave of fundamental pattern with $a = 1, b = 3/2, c = 1, d_0 = 1, \omega = 0, s_1 = 0, s_2 = 0$.

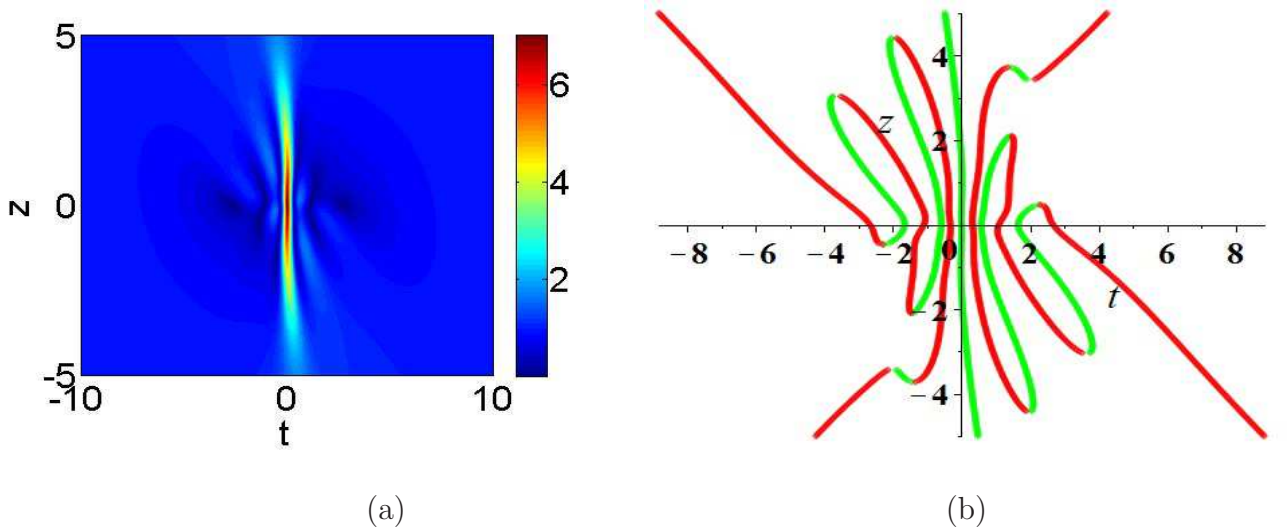


Fig. 7: (a) Density plot and (b) trace of the third-order rogue wave of fundamental pattern with $a = 1, b = -3/2, c = 1, d_0 = 1, \omega = 0, s_1 = 0, s_2 = 0$.

3.3. W-shaped soliton

As is announced before, when letting the MI growth rate tend to zero under the zero-frequency MS region, one can bring about the state transition from rogue wave to W-shaped soliton. For that purpose, we take

$$b = b_s|_{\kappa=0} = \frac{2(2\omega - a)d_0}{3a^2 - 12a\omega + 4c^2 + 12\omega^2}. \quad (16)$$

Then through the direct substitution of Eq. (16) into Eq. (12), we can define the motions of the first-order W-shaped soliton' hump and valleys analytically

$$T'_h = -K'z, \quad (17)$$

and

$$T'_v = -K'z \pm \frac{\sqrt{3}}{2}, \quad (18)$$

where

$$K' = \frac{d_0}{3a^2 - 12a\omega + 4c^2 + 12\omega^2}.$$

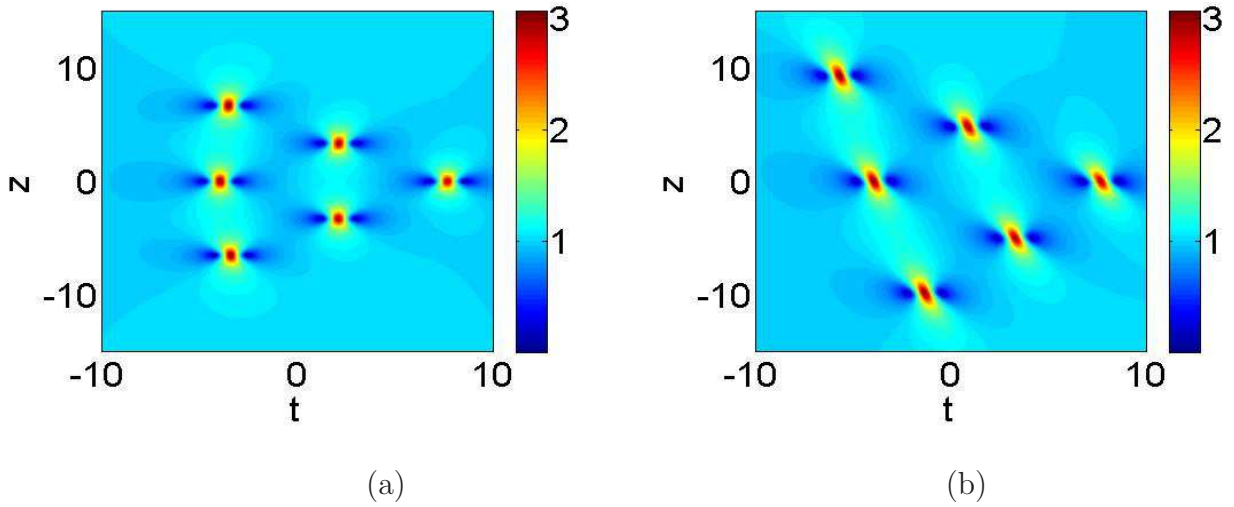


Fig. 8: (a), (b) Density plots of the third-order rogue waves of triangular pattern by choosing $b = 3/2$ and $b = -3/2$ with $a = 1, c = 1, d_0 = 1, \omega = 0, s_1 = 100, s_2 = 0$.

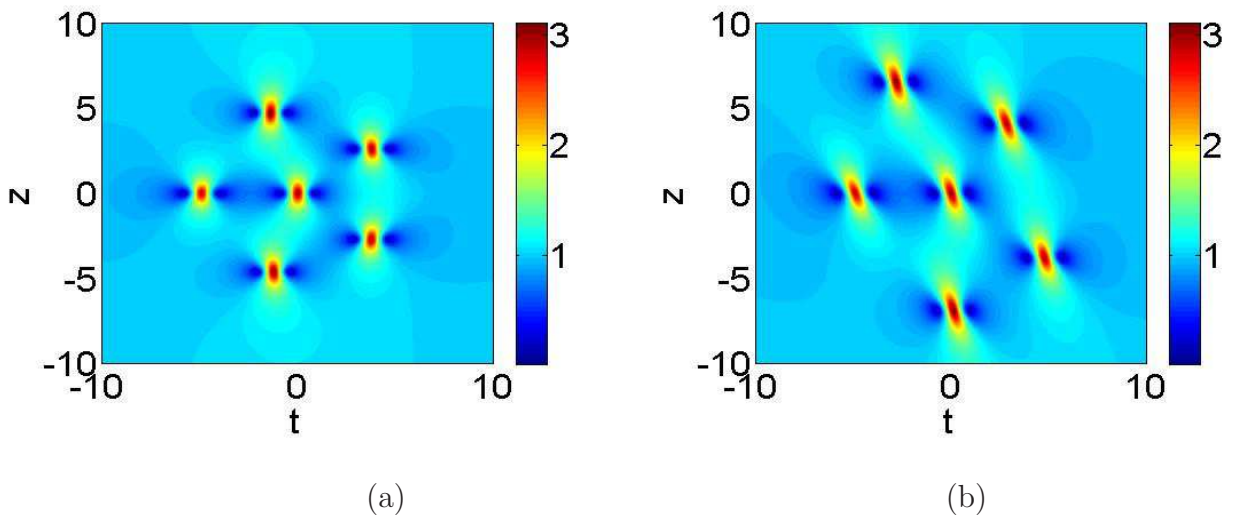


Fig. 9: (a), (b) Density plots of the third-order rogue waves of circular pattern by choosing $b = 3/2$ and $b = -3/2$ with $a = 1, c = 1, d_0 = 1, \omega = 0, s_1 = 0, s_2 = 1000$.

Here, it is facile to verify that the maximum amplitude of the first-order W-shaped soliton is 3 and arrives at $t + K'z = 0$, and the minimum value of it is 0 and occurs at $t + K'z = \pm\sqrt{3}/2$. By solving $K' = 0$ we get $d_0 = 0$, then in this circumstance, the trajectories of the hump and that of the valleys of the W-shaped soliton are stationary in the z dimension. In other words, the explicit soliton solution and its trace are independent on the temporal variable z . At this point, we call this type of the soliton as the stationary W-shaped soliton, see Fig. 10(a). By contrast, if $d_0 \neq 0$, the explicit soliton solution depends on both t and z , and its trace is determined by Eqs. (17) and (18). The soliton in this circumstance is viewed as the nonstationary W-shaped soliton, see Fig. 10(b).

Particularly, we need to remark that, the nonstationary W-shaped soliton can only exist in the multiple SIT system (2). For the single SIT system (1), the reduction condition $e \rightarrow 0, M \rightarrow 0$

allows

$$b = \frac{d_0}{2\omega - a}$$

in the general plane-wave solution (7). By taking into account of the above equation alongside with Eq. (16) we have $d_0 = 0$. Thus, there only exists the stationary W-shaped soliton in system (1), whereas for the nonstationary one it is impossible to emerge. The stationary W-shaped solitons in system (1) have been recently studied by Wang [14], and the above fact can also be readily proved through the direct MI analysis of system (1).

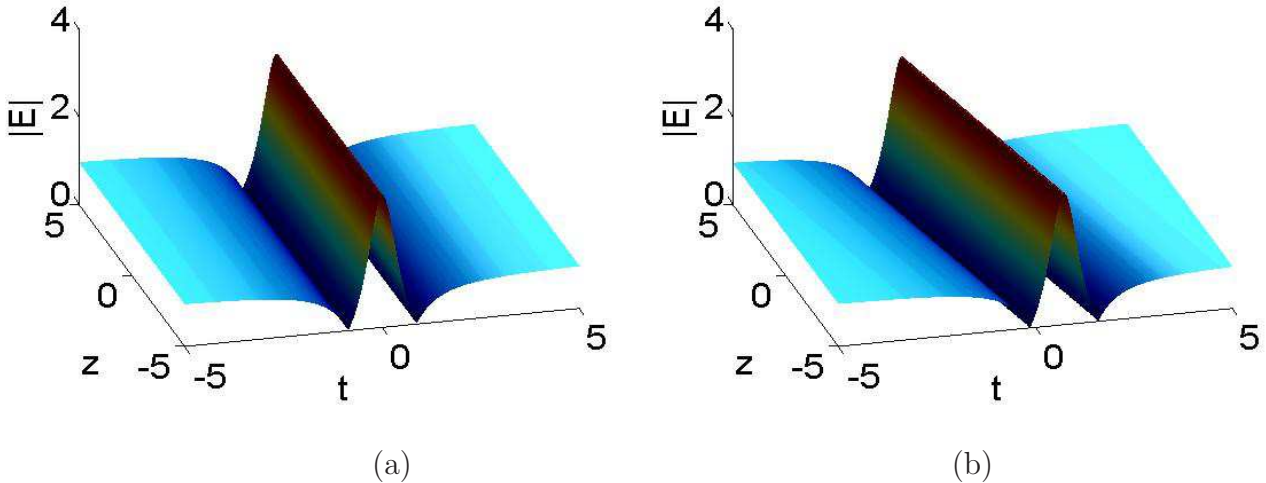


Fig. 10: (a), (b) Density plots of the first-order stationary and nonstationary W-shaped solitons given by Eq. (12) with $d_0 = 0, b = 0, a = 1, c = 1, \omega = 0$ and $d_0 = 1, b = -2/7, a = 1, c = 1, \omega = 0$.

Next, under the special choice of $a = 1, c = 1, \omega = 0$ and $s_1 = 0$, we can employ Eq. (8) with $N = 2$ and Eq. (16) to obtain a second-order W-shaped soliton solution containing the important free parameter d_0 , viz.

$$E[2]' = e^{i\theta} \frac{F_2' + iG_2'}{D_2'}, \quad (19)$$

where the corresponding polynomials are explicitly given in appendix B.

By taking $d_0 = 0$, as is exhibited in Fig. 11(a), there are three humps in the temporal-spatial plane, the corresponding amplitudes are 5 and 1, and occur at $t = 0$ and $t = \pm 0.8660$. The number of the zero-amplitude valleys is four and they arrive at $t = \pm 1.7571$ and $t = \pm 0.4650$. For the nonstationary case of $d_0 \neq 0$, we display that in Fig. 11(b), two first-order nonstationary W-shaped solitons interacted with each other, and the maximum amplitude of the second-order W-shaped soliton is 5 and is localized at $(0, 0)$.

For the third-order W-shaped soliton, we omit presenting the lengthy explicit solution with form of the mixture of higher-order rational polynomials and exponential function. As is shown in Fig. 12(a), there are five humps in the $t - z$ distribution plane, viz., $t = 0, t = \pm 1.6562$ and $t = \pm 0.5833$, and their amplitudes are 5, 0.5139 and 1.8991. Moreover, the six valleys are reached at $t = \pm 2.6714, t = \pm 1.0931$ and $t = \pm 0.3238$, and their amplitudes are all 0. Based on these facts, we can infer that the N th-order stationary W-shaped soliton has $2N - 1$ humps and $2N$ valleys. On the other hand, the third-order nonstationary W-shaped soliton is exhibited in Fig. 12(b), the maximum amplitude of it is 7 and arrives at $(0, 0)$.

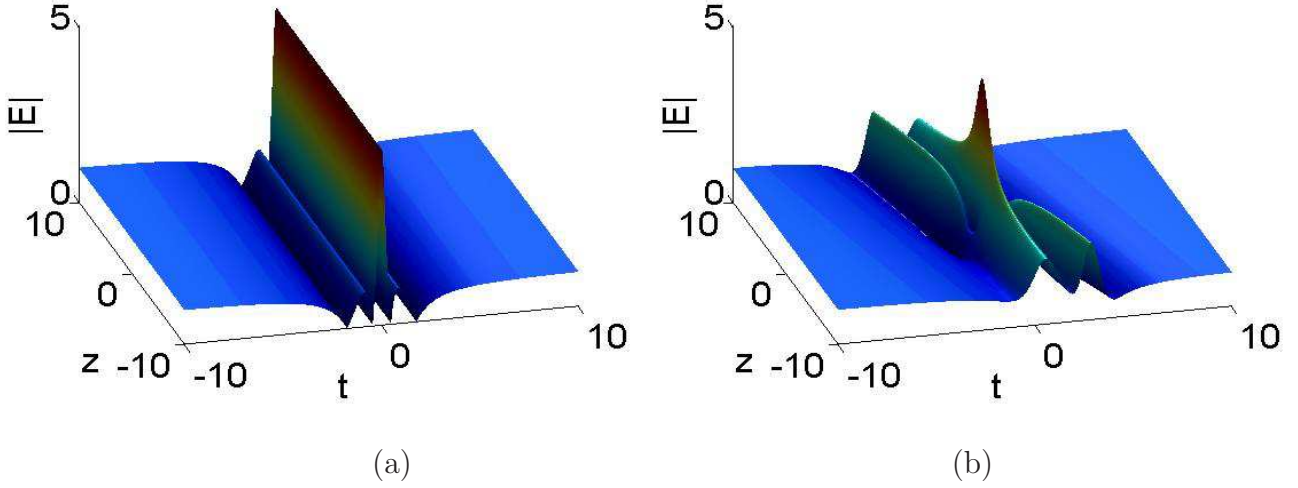


Fig. 11: (a), (b) Density plots of the second-order stationary and nonstationary W-shaped solitons given by Eq. (19) with $d_0 = 0$ and $d_0 = 1$.

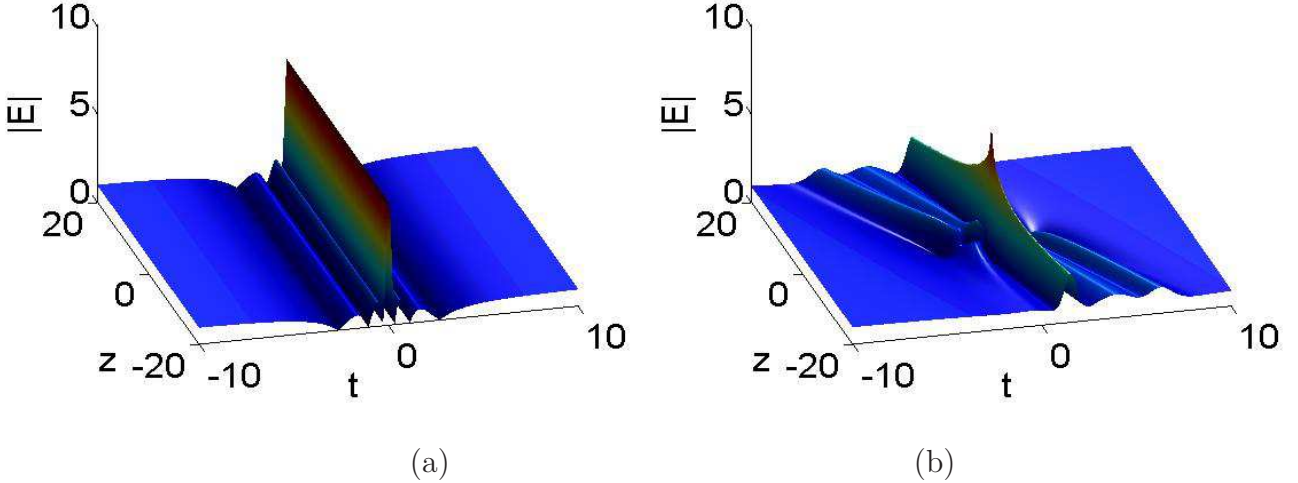


Fig. 12: (a), (b) Density plots of the third-order stationary and nonstationary W-shaped solitons by choosing $d_0 = 0, b = 0$ and $d_0 = 1, b = -2/7$ with $a = 1, c = 1, \omega = 0, s_1 = 0, s_2 = 0$.

4. Spectrum analysis and energy of the rogue wave solution

It is recently recognized that spectrum analysis is a meaningful tool for the prediction and excitation of the rogue wave [40]. Therefore, in this section, we try to perform the spectrum analysis of the first-order rogue wave solution. In order to more conveniently reveal the relationship between the spectrum and state transition condition in comparison with Figs. 1(a), 2(a) and 10(b), we consider the following rogue wave solution with the special choice of $a = 1, c = 1, d_0 = 1$ and $\omega = 0$ in Eq. (12), namely,

$$E[1]_s = -\frac{100t^2 - (16b - 24)zt + (32b^2 + 16b + 4)z^2 - 75 + i(112b + 32)z}{100t^2 - (16b - 24)zt + (32b^2 + 16b + 4)z^2 + 25} e^{i(t+bz)}. \quad (20)$$

Then the spectrum of Eq. (20) yields

$$|F(\lambda, z)| = \left| \frac{1}{\sqrt{2\pi}} \int_{-\infty}^{\infty} E[1]_s(t, z) e^{i\lambda t} dt \right| = \sqrt{2\pi} \exp \left(-\frac{\sqrt{16(7b+2)^2 z^2 + 625}}{50} |\lambda'| \right), \quad (21)$$

where $\lambda' = \lambda - 1$.

Given this definition, one can easily find that when $b \neq -2/7$, the spectrum is nothing but that of the standard Peregrine soliton which features a triangular shape [40]. We observe that, in Figs. 13(a) and 13(b), the spectrum of the rogue wave solution with $b = -3/2$ gets broadened at the maximally compressed point ($z = 0$) in contrast with that of the rogue wave solution with $b = 3/2$. Further, when taking $b = -2/7$, the spectrum of the nonstationary W-shaped soliton becomes stable and broad, see Fig. 13(c).

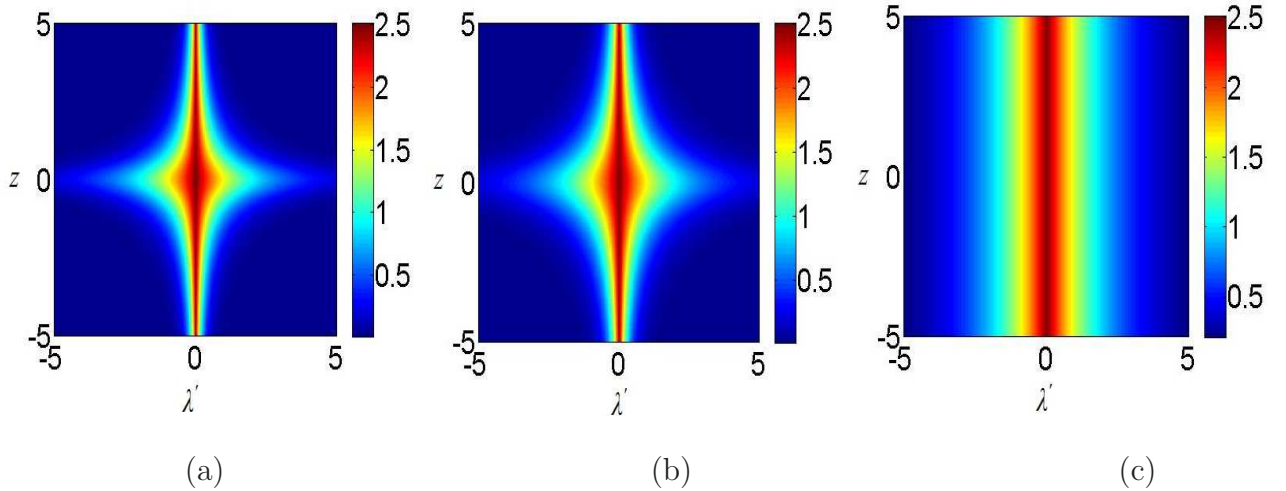


Fig. 13: Spectrum dynamics $|F(\lambda, z)|$ with (a) $b = 3/2$, (b) $b = -3/2$ and (c) $b = -2/7$.

The evolutionary process of the spectrum is completely coincide with the state transition presented in Figs. 1(a), 2(a) and 10(b). In addition, we can define the energy of the rogue wave pulse:

$$E_{pulse}(z) = \int_{-\infty}^{+\infty} |E[1]_s(t, z) - E[1]_s(\pm\infty, z)|^2 dt = \frac{100\pi}{\sqrt{16(7b+2)^2 z^2 + 625}}. \quad (22)$$

The free parameter b controls the wave width of the energy function. When $b = -2/7$, the rogue wave is converted to W-shaped soliton, and the energy becomes a constant, i.e. 4π . This fact further verifies the state transition condition obtained through the MI analysis.

5. Conclusion and discussions

In conclusion, by using the generalized DT method, we proposed a compact determinant representation for arbitrary N th-order rational solution of the multiple SIT system, which plays an important role in enhancement of the amplification and control of optical waves compared to the single SIT system. By virtue of the rational solution, MI and the trace analysis method, we put forward the optical rogue wave, as well as the stationary and nonstationary W-shaped solitons structures from first to third order. We found that the nonstationary W-shaped solitons could only exist in the multiple SIT system instead of the single case. Further, we demonstrated that the evolutionary processes of the spectrum and energy of the rogue wave solution were completely coincide with the state transition condition given by the MI analysis.

Besides, on the one hand, we note that the N th-order Akhmediev breather solution, multi-peak solution and periodic solution of the multiple SIT system can be obtained by slightly adjusting Eq. (8) with the small complex parameter f being chosen as the nonzero constant. On the other hand, the results presented in this paper can be directly generalized to the resonant erbium-doped fiber system described by the NLS-multiple SIT equations. These problems are also interesting and we will summarize the corresponding results in our recent papers.

Acknowledgment

One of the authors X. Wang would like to thank Professor Y. Chen, Doctor L.M. Ling, L.C. Zhao and L. Wang for their valuable suggestions and discussions.

Appendix A: Polynomials in Eq. (15)

$$\begin{aligned}
F_2 &= 1000000t^6 - 2250000t^4 - 2812500t^2 - 384(2b-3)(8b^2+4b+1)^2z^5t + 64(8b^2+4b+1)^3z^6 \\
&\quad + (-256(2b-3)(608b^2+276b+93)t^3 + (912384b^3 - 73728b^2 - 33408b + 16704)t)z^3 \\
&\quad + (4800(216b^2+52b+61)t^4 - 36000(32b^2-4b-1)t^2 + 2412000b^2 + 2142000b + 607500)z^2 \\
&\quad + (192(216b^2+52b+61)(8b^2+4b+1)t^2 - 1483776b^4 - 1625088b^3 - 764928b^2 - 160896b \\
&\quad - 11280)z^4 + (-240000(2b-3)t^5 + 24000(-2b-37)t^3 + 9000(-142b-27)t)z + 703125, \\
G_2 &= -3072(7b+2)(2b-3)(8b^2+4b+1)z^4t + 768(7b+2)(8b^2+4b+1)^2z^5 + (1536(7b+2) \\
&\quad \times (208b^2+76b+43)t^2 - 2896896b^3 - 2631168b^2 - 920448b - 82176)z^3 + (-76800(2b-3) \\
&\quad \times (7b+2)t^3 + 288000(6b^2+3b+2)t)z^2 + (480000(7b+2)t^4 - 144000(-37b-22)t^2 \\
&\quad - 558000b + 252000)z, \\
D_2 &= 1000000t^6 + 750000t^4 + 1687500t^2 - 384(2b-3)(8b^2+4b+1)^2z^5t + 64(8b^2+4b+1)^3z^6 \\
&\quad + (-256(2b-3)(608b^2+276b+93)t^3 + (3072b^3 + 792576b^2 + 625536b + 148032)t)z^3 \\
&\quad + (4800(216b^2+52b+61)t^4 + 36000(128b^2+84b+21)t^2 + 684000b^2 + 558000b + 211500)z^2 \\
&\quad + (192(216b^2+52b+61)(8b^2+4b+1)t^2 + 48(24b^2-12b-11)^2)z^4 + (-240000(2b-3)t^5 \\
&\quad - 24000(42b-23)t^3 - 9000(-34b-29)t)z + 140625.
\end{aligned}$$

Appendix B: Polynomials in Eq. (19)

$$\begin{aligned}
F'_2 &= 1000000t^6 - 2250000t^4 - 150000000t^3 - 2812500t^2 + \frac{6000000}{16807}d_0^5z^5t - 337500000t \\
&\quad + \left(\frac{15000000}{2401}d_0^4t^2 + \frac{90000}{343}d_0^4 \right) z^4 + \left(\frac{20000000}{343}d_0^3t^3 - \frac{360000}{343}d_0^3t - \frac{150000000}{343}d_0^3 \right) z^3 \\
&\quad + \left(\frac{15000000}{49}d_0^2t^4 - \frac{4860000}{49}d_0^2t^2 - \frac{450000000}{49}d_0^2t + \frac{9427500}{49}d_0^2 \right) z^2 + \frac{1000000}{117649}d_0^6z^6 \\
&\quad + \left(\frac{6000000}{7}d_0t^5 - \frac{6120000}{7}d_0t^3 - \frac{450000000}{7}d_0t^2 + \frac{855000}{7}d_0t - \frac{553500000}{7}d_0 \right) z \\
&\quad + 5625703125,
\end{aligned}$$

$$\begin{aligned}
G'_2 &= \frac{23040000}{49}d_0^2z^2t + \frac{11520000}{343}d_0^3z^3 + \left(\frac{11520000}{7}d_0t^2 + \frac{2880000}{7}d_0 \right) z, \\
D'_2 &= 1000000t^6 + 750000t^4 - 150000000t^3 + 1687500t^2 + \frac{6000000}{16807}d_0^5z^5t + 112500000t \\
&+ \left(\frac{15000000}{2401}d_0^4t^2 + \frac{3630000}{2401}d_0^4 \right) z^4 + \left(\frac{20000000}{343}d_0^3t^3 + \frac{11640000}{343}d_0^3t - \frac{150000000}{343}d_0^3 \right) z^3 \\
&+ \left(\frac{150000000}{49}d_0^2t^4 + \frac{13140000}{49}d_0^2t^2 - \frac{450000000}{49}d_0^2t + \frac{5287500}{49}d_0^2 \right) z^2 + \frac{1000000}{117649}d_0^6z^6 \\
&+ \left(\frac{6000000}{7}d_0t^5 + 840000d_0t^3 - \frac{450000000}{7}d_0t^2 + \frac{1215000}{7}d_0t - \frac{103500000}{7}d_0 \right) z \\
&+ 5625140625.
\end{aligned}$$

References

References

- [1] J. Downing, Fiber Optic Communications, Cengage Learning, 2004.
- [2] G.P. Agrawal, Nonlinear fiber optics, Academic press, 2007.
- [3] A. Hasegawa, F. Tappert, Appl. Phys. Lett. 23 (1973) 142-144.
- [4] S. L. McCall, E. L. Hahn, Phys. Rev. Lett. 18 (1967) 908-911.
- [5] G.L. Lamb, Phys. Rev. Lett. 31 (1973) 196-199.
- [6] A.M. Kamchatno, M.V. Pavlov, J. Phys. A 28 (1995) 3279-3288.
- [7] S. Coleman, Phys. Rev. D 11 (1975) 2088-2097.
- [8] M.J. Ablowitz, D.J. Kaup, A.C. Newell, J. Math. Phys. 15 (1974) 1852-1858.
- [9] I.R. Gabitov, A.V. Mikhailov, V.E. Zakharov, JETP Lett. 37 (1983) 279-282.
- [10] V.B. Matveev, M.A. Salle, Darboux transformations and solitons, Springer, 1991.
- [11] J.S. He, S.W. Xu, K. Porsezian, Y. Cheng, P.T. Dinda, Phys. Rev. E 93 (2016) 062201.
- [12] X. Wang, Y.Q. Li, F. Huang, Y. Chen, Commun. Nonlinear Sci. Numer. Simulat. 20 (2015) 434-442.
- [13] X.Y. Wen, Z.Y. Yan, Chaos 25 (2015) 123115.
- [14] L. Wang, Z.Q. Wang, J.H. Zhang, F.H. Qi, M. Li, arXiv:1601.07029v1 (2016).
- [15] A. Kundu, Theor. Math. Phys. 167 (2011) 800-810.
- [16] K. Dysthe, H.E. Krogstad, P. Müller, Annu. Rev. Fluid Mech. 40 (2008) 287-310.
- [17] D.R. Solli, C. Ropers, P. Koonath, B. Jalali, Nature 450 (2007) 1054-1057.
- [18] Y.V. Bludov, V.V. Konotop, N. Akhmediev, Phys. Rev. A 80 (2009) 033610.
- [19] W.M. Moslem, P.K. Shukla, B. Eliasson, Eur. Phys. Lett. 96 (2011) 25002.
- [20] L. Wen, L. Li, Z.D. Li, S.W. Song, X.F. Zhang, W.M. Liu, Eur. Phys. J. D 64 (2011) 473-478.
- [21] D.H. Peregrine, J. Austral. Math. Soc. B: Appl. Math. 25 (1983) 16-43.
- [22] A. Ankiewicz, D.J. Kedziora, N. Akhmediev, Phys. Lett. A 373 (2011) 2782-2785.
- [23] A. Chabchoub, N. Hoffmann, M. Onorato, N. Akhmediev, Phys. Rev. X 2 (2012) 011015.
- [24] A. Ankiewicz, J.M. Soto-Crespo, N. Akhmediev, Phys. Rev. E 81 (2010) 046602.
- [25] S.H. Chen, Phys. Rev. E 88 (2013) 023202.
- [26] F. Baronio, A. Degasperis, M. Conforti, S. Wabnitz, Phys. Rev. Lett. 109 (2012) 044102.
- [27] L.M. Ling, B.L. Guo, L.C. Zhao, Phys. Rev. E 89 (2014) 041201.
- [28] X. Wang, Y.Q. Li, Y. Chen, Wave Motion 51 (2014) 1149.
- [29] A. Chowdury, A. Ankiewicz, N. Akhmediev, Proc. Proc. R. Soc. A. 471 (2015) 20150130.
- [30] C. Liu, Z.Y. Yang, L.C. Zhao, W.L. Yang, Ann. Phys. 362 (2015) 130-138.
- [31] C. Liu, Z.Y. Yang, L.C. Zhao, W.L. Yang, Phys. Rev. E 91 (2015) 022904.
- [32] Y. Ren, Z.Y. Yang, C. Liu, W.L. Yang, Phys. Lett. A 379 (2015) 2991-2994.
- [33] B.L. Guo, L.M. Ling, Q.P. Liu, Phys. Rev. E 85 (2012) 026607.
- [34] B.L. Guo, L.M. Ling, Q.P. Liu, Stud. Appl. Math. 130 (2013) 317.

- [35] L.M. Ling, L.C. Zhao, Phys. Rev. E 88 (2014) 043201.
- [36] X. Wang, B. Yang, Y. Chen, Y.Q. Yang, Phys. Scr. 89 (2014) 095210.
- [37] F. Baronio, S.H. Chen, P. Grelu, S. Wabnitz, M. Conforti, Phys. Rev. A 91 (2015) 033804.
- [38] L. Wang et al., Phys. Rev. E 93 (2016) 012214.
- [39] C. Bayindir, Phys. Rev. E 93 (2016) 032201.
- [40] N. Akhmediev, A. Ankiewicz, J.M. Soto-Crespo, J.M. Dudley, Phys. Lett. A 375 (2011) 541-544.